Nonintrusive Measurements for Detecting Progressive Equipment Faults

Daisy H. Green, *Member, IEEE*, Devin W. Quinn, Samuel Madden,
Peter A. Lindahl, *Senior Member, IEEE*, and Steven B. Leeb, *Fellow, IEEE*

***Abstract*— The gradual environmental degradation of materials can lead to corrosion and mechanical failures of electrical loads. Vibration and corrosion both contribute to the failure of electrical connections and conductors, and electrical arcs destroy materials in ways that enhance the opportunities for further damage. These failures lead to loss of system capability and the possibility of electrical fires. The signatures of these impending electrical failures, which may occur over weeks or months, can be detected in many systems through nonintrusive electrical monitoring. This article demonstrates techniques for decoding the type of electrical signatures that lead to progressive failure. Example applications of these techniques are illustrated with observations of the degradation and failure of copper-sheathed jacket water (JW) heaters aboard a United States Coast Guard (USCG) vessel. Electrical, material, and vibration analysis are presented to demonstrate the basis for diagnostic electrical signatures.**

***Index Terms*— Condition-based maintenance, corrosion, fault detection, nonintrusive load monitoring, power monitoring, root-cause analysis.**

I. INTRODUCTION

INDUSTRIAL processes rely on materials that are susceptible to corrosion and mechanical failure [1]–[3]. For instance, heat exchangers in industrial facilities often exploit the high thermal conductivity of copper. In high-stress environments, copper structures are susceptible to corrosion and cracking. The copper sheathing of a heating element can degrade to the point of failure and expose the electrically active heating elements. Prior to complete system failure, degradation can lead to arcing and water intrusion. Early detection can prevent service delays and hazards, such as electrical fires. However, the detection and evaluation of corrosion in critical structures remain a significant maintenance and repair challenge [4].

The typical construction of large marine diesel engines incorporates a jacket water (JW) system to provide engine cooling while operating. The JW acts as a heat absorbing medium that removes heat from engine components and releases it to the environment through a heat exchanger. Thermostatic valves often regulate the flow of JW through the heat exchanger based on engine temperature. While the engine is not running, the JW system also plays a significant role in maintaining uniform engine temperature by circulating water through resistive heaters. This minimizes time to reach standard operating temperatures upon startup. The United States Coast Guard's (USCG) Medium Endurance Cutter (MEC) 270 fleet uses copper-sheathed heaters in the main propulsion diesel engine (MPDE) JW system [5].

Per manufacturer recommendations, the USCG conducts semi-annual visual and electrical state examination of the three-phase JW heaters and control systems used on the MPDE. Changes in operation or faults related to the JW heater appear as changes in the electrical power consumption. Electrical monitoring can detect degradation and potential fire hazards at an earlier stage than scheduled inspections, thus reducing the overall risk of a disastrous event. Equipment can be monitored individually or nonintrusively (as a collection of loads). A nonintrusive load monitor (NILM) is a convenient approach for electrical monitoring, as it requires only a single set of current and voltage sensors at the feeder to an electrical panel to monitor all downstream loads [6]. A NILM uses identification of transient signatures, such as when a load energizes or changes state, to determine individual load operation [7], [8]. With the correct physical interpretation of measurements, nonintrusive electrical data can be used for monitoring and diagnostics of individual equipment. The challenge, however, is ensuring correct results even amidst load degradation and fault conditions.

Most nonintrusive load monitoring research assumes training data are forever representative of new data, without regard to changing load behavior [9], [10]. However, practical data are not static. A load's electrical characteristics, such as its steady-state and inrush transient peak, can change over time [11]. Some variability is expected even for a healthy load, for example, due to variations in the turn-on angle and voltage amplitude. Variability can also arise from changing environmental conditions, machinery aging and wear, or an underlying fault condition. The existing work for fault detection and diagnostics with aggregate electrical monitoring is mainly limited to load timing faults, such as short cycling or elongated duty cycle, but not drifting transient and steady-state behavior [12]–[14]. Current work that uses changes in steady-state power as a diagnostic metric is limited by the availability of historical data for creating warning threshold levels [5], [10], [15], [16]. If degraded transient signatures can be identified and tracked, it would further

Manuscript received 6 April 2022; revised 12 June 2022; accepted 1 July 2022. Date of publication 21 July 2022; date of current version 29 July 2022. This work was supported in part by the Office of Naval Research NEPTUNE Program and in part by The Grainger Foundation. The Associate Editor coordinating the review process was Dr. Zhibin Zhao. *(Corresponding author: Daisy H. Green.)*

Daisy H. Green, Devin W. Quinn, and Steven B. Leeb are with the Department of Electrical Engineering and Computer Science, Massachusetts Institute of Technology, Cambridge, MA 02139 USA (e-mail: dhgreen@mit.edu).

Samuel Madden and Peter A. Lindahl are with Exponent, Inc., Natick, MA 01760 USA.

Digital Object Identifier 10.1109/TIM.2022.3193178

Fig. 1. Three-phase JW heater. New heater (top) and heater with significant corrosion and degradation of heating elements (bottom).

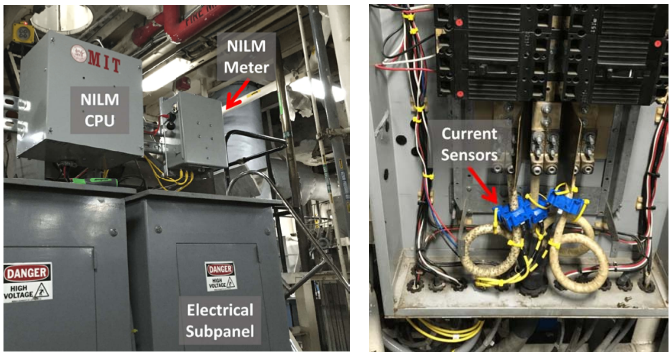

(a) (b)

Fig. 2. NILM installation on USCGC SPENCER. (a) NILM CPU and meter boxes mounted above the monitored electrical panel. (b) Electrical panel interior with installed currents sensors.

enable the use of nonintrusive load monitoring for detecting incipient failures and permitting condition-based, instead of scheduled maintenance.

In the results presented here, nonintrusive electrical monitoring reveals the degradation signatures of USCG MPDE JW heaters observed from two MECs, SPENCER and ESCANABA. The connection between the observed electrical measurements and the actual physical task performed by the JW heater is presented to guide the detection of JW heater equipment faults. Since the degradation detection techniques demonstrated in this article are based on physical understanding, it enables the detection of incipient failures without requiring extensive historical data of the fault conditions. After detection of degraded power signatures, physical inspection of the heaters revealed significant corrosion and damage, including arcing, melting, and cracking of the heating elements. Fig. 1 shows a comparison of a new JW heater and a degraded JW heater after being removed from the engine block. Material, stress, and vibration analysis of the observed field failures are presented to demonstrate the connection between observed electrical failure signatures and root-cause failure and degradation mechanisms.

II. Measurement Hardware and Preprocessing

USCG cutters (USCGCs) SPENCER and ESCANABA are 440/254-V ungrounded delta-configured distribution systems with a wye-configured source generator. NILMs were installed to monitor the port and starboard electrical subpanels of the engine room on each ship. These panels supply power to auxiliary equipment necessary for maintaining operational readiness of the ships' main diesel engines and ship-service diesel generators. The panels also supply power to several other loads critical to ship operation [12]. Fig. 2 shows a NILM installation on USCGC SPENCER. The NILMs on SPENCER and ESCANABA measure three line currents and three line-to-line voltages. In Fig. 2(a), the NILM computer processing and storage unit (CPU) and NILM meter hardware boxes are mounted directly above the monitored subpanel. The NILM meter contains the analog circuitry and the data acquisition (DAQ) hardware. The DAQ hardware for these shipboard installations is the LabJack UE9 [17], which obtains data at a 12-bit input resolution. An analog-to-digital converter (ADC) samples the voltages and currents at 8 kHz. The current sensing hardware is the LEM LF-305, as shown in Fig. 2(b), which can measure a current up to 300 A. The discrete current signal for each phase is $i_\phi[n]$, where $\phi \in \{a, b, c\}$. For a quantizer that operates between $-I_{\max}$ and $+I_{\max}$, and with $I_{\max}$ aligned to the maximum measurable current (i.e., 300 A), the least significant bit (LSB) of quantized input current is 0.146 A. The NILM CPU box contains a Linux-based personal computer, which runs the NILM software [18].

The voltage and current data are preprocessed into real power, reactive power, and higher-order harmonics using the Sinefit algorithm [19]. This preprocessing compresses the high-rate raw current and voltage data to an output frequency congruent with the line frequency (i.e., 60 Hz). The currents are converted to spectral envelopes, i.e., a measure of harmonic content averaged over every ac line cycle [19], [20]. Spectral envelopes of the currents are computed over sliding windows of the input signal phase-aligned with a reference voltage, $v[n] = V_{\text{pk}} \sin(2\pi n/N)$. Here, the peak magnitude is $V_{\text{pk}} = \sqrt{2}$ V, where $V = 254$ is the rms line-to-neutral voltage magnitude. One period is length $N = f_s/f_0$ samples, where f_s is the sampling frequency, and f_0 is the line frequency. Under the assumption that the voltages are relatively "stiff" and harmonic-free, a single measured line-to-line voltage is used as the phase reference, and the corresponding phase rotation corrections are applied. For a current $i[n]$, in which the current is phase-aligned with the reference voltage, the in-phase and quadrature components of the rms current envelope at line frequency harmonic k are

$$I_k^I = \frac{\sqrt{2}}{N} \sum_{n=0}^{N-1} i[n] \sin\left(k \frac{2\pi n}{N}\right) \tag{1}$$

$$I_k^Q = -\frac{\sqrt{2}}{N} \sum_{n=0}^{N-1} i[n] \cos\left(k \frac{2\pi n}{N}\right). \tag{2}$$

These are equivalent to the imaginary and real components, respectively, of the discrete Fourier transform (DFT) of $i[n]$,

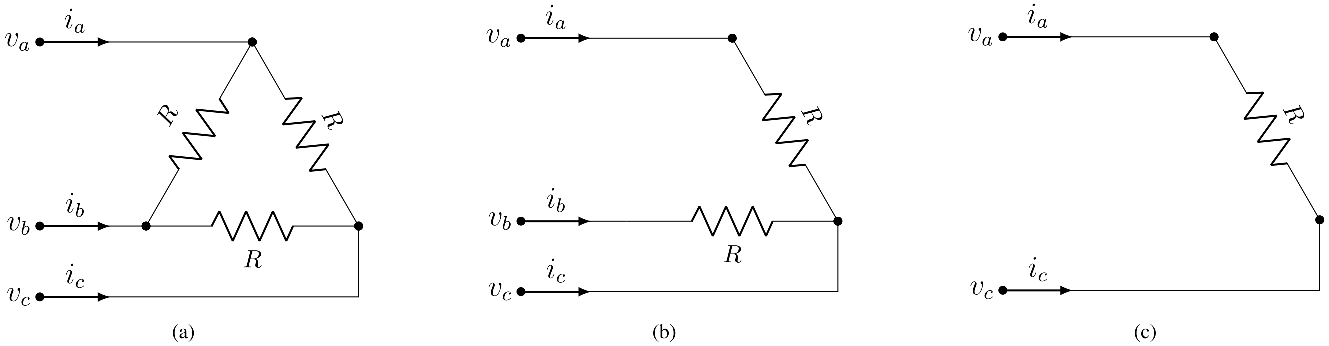

Fig. 3. Three different load connections for a delta-connected system. (a) Three phase. (b) Two phase. (c) Single phase.

scaled by $-\sqrt{2}/N$. Since the voltage phase reference is line-to-line, phase rotations of 30°, 150°, and 270° are applied to the complex DFT coefficient for phases a, b, and c, respectively. It is also possible for there to be a phase shift of 180° of the voltages with respect to the currents. In which case, phase rotations of 210°, 330°, and 90° are applied instead. The in-phase and quadrature spectral envelopes for each phase are represented as $I^I_{\phi k}$ and $I^Q_{\phi k}$, respectively. The fundamental current component is used to calculate the real power (P) and reactive power (Q) streams for each phase

$$P_\phi = V I^I_{\phi 1}, \quad Q_\phi = V I^Q_{\phi 1}. \tag{3}$$

Section III presents healthy and degraded JW heater electrical signatures.

III. ELECTRICAL ANALYSIS

Both the port and starboard subpanels supply power to an MPDE JW heater system, consisting of two symmetrical delta-connected 4.5-kW heaters on either side of the engine block. That is, there are four MPDE JW heaters total per ship. The two 4.5-kW heaters of the JW system are controlled by a single thermocouple and energize simultaneously. When healthy, they appear to the NILM as a single 9-kW resistive load, with 3 kW per phase.

An electrical load can experience a numerous set of failures with associated sets of electrical transient signatures. These failure signatures can be explained by the physics of load operation, as demonstrated in this section. A NILM can be trained to recognize diagnostic signatures in the time-series streams of real power, reactive power, and higher-order current harmonic content. In this section, it is specifically demonstrated how successive failures in the individual heating elements are visible in the aggregate electrical stream as a series of degradation events.

A. Line-to-Line Open Circuit Fault

Corrosion and damaged sheathing can result in a failed heating element and a line-to-line open circuit. With two line-to-line open-circuited heating elements, the load becomes a single-phase line-to-line load. Fig. 3 shows diagrams for these three scenarios in a delta-connected system: a three-phase load, two-phase load, and single-phase load, with the resistance R representing the resistance of a single heating element. The NILM can be trained to recognize a failed heating element, since a simultaneous failure of all three heating elements is not typically observed. Fig. 4 shows the line currents for simulations of the three scenarios in Fig. 3 with resistance $R = 129\ \Omega$ (corresponding to 1.5 kW per delta phase on a 440/254-V ship system). The currents in Fig. 4 emulate the JW heater in a healthy state [Fig. 4(a)] and in progressively faulty states [Fig. 4(b) and (c)].

A line-to-line open circuit manifests as a reduction in magnitude and phase shift in two of the line currents. This results in a decrease in P on two phases and changes in Q on two phases of equal magnitude but opposite sign. Specifically, for a three-phase heater that starts with rated power P_r (e.g., 4.5 kW for the JW heater), given the scenario in Fig. 3(b), the real power on each phase is: $P_a = P_b = P_r/6$, and $P_c = P_r/3$. The reactive power on each phase is: $Q_a = P_r/(6\sqrt{3})$, $Q_b = -P_r/(6\sqrt{3})$, and $Q_c = 0$. The total power is $P_{\text{total}} = (2/3)P_r$ and $Q_{\text{total}} = 0$, as expected, since there are only two operational heating elements. Fig. 5 shows the simulated power streams for a JW heater turning on and off, for the case of an open-circuited phase ab heating element.

Since the NILM is measuring two JW heaters in tandem, the NILM can detect an open circuit failure of any of the six heating elements. That is, only after the sixth consecutive failed heating element will the JW heating system have a complete system failure. These events are insidious, as the JW heating system can still warm the JW by operating the remaining heater elements. The heaters may also operate longer, but as long as the remaining heating capacity is sufficient for maintaining the required water temperature, this is invisible to the ship's watchstander as it is a fully automated system.

Open circuiting of the heating elements has been observed on both ships in various stages of degradation, with the observed time between consecutive open circuit failures ranging from hours to months. For example, Fig. 6 shows the real and reactive power on transient for four different measured scenarios of the port-side JW heater system on SPENCER. The leftmost plot is of two healthy heaters, so the step change in power when the load turns on is ≈3 kW of real power and zero reactive power on each phase. The second plot has a single degraded bc heating element. The third plot has two degraded

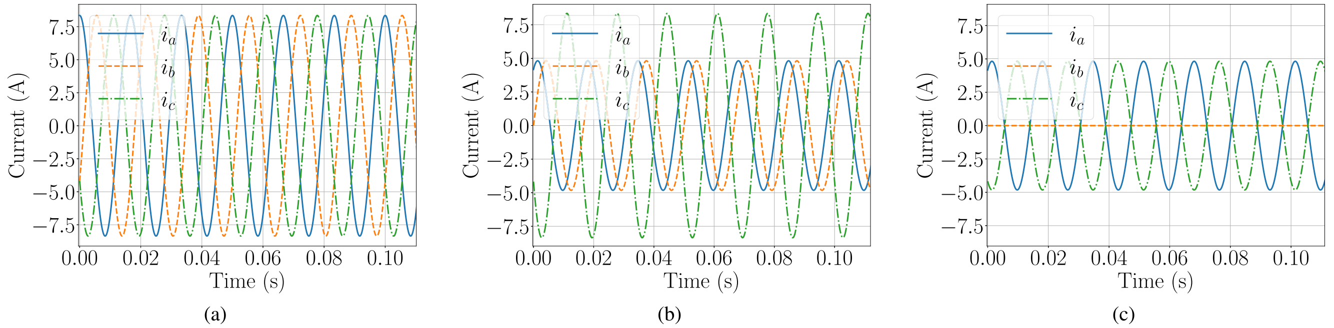

Fig. 4. Line currents for three different load connections in a delta-connected system. (a) Three phase. (b) Two phase. (c) Single phase.

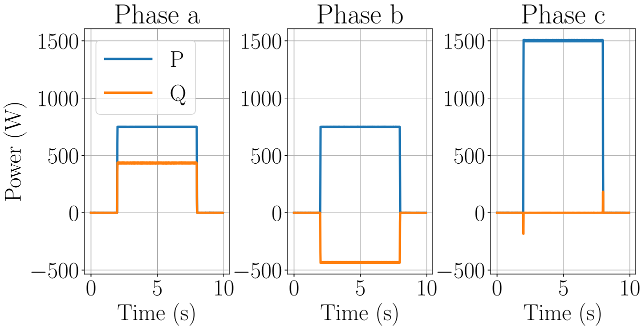

Fig. 5. Power per phase of a simulated delta-connected heater with an open circuit of the phase *ab* heating element.

heating elements: one *bc* element and one *ca* element. The rightmost plot has four degraded heating elements: both *bc* elements and both *ca* elements. In this final state, only two of the six heating elements are operational, and the heating system is only drawing one-third of the rated power. Open circuit failures of the heating elements indicate that there may be damage to the heating coil, and that the heater may be at risk for other damaging failures.

B. High Current Arcing Fault

Damaged sheathing or exposed wiring can cause arcing or direct shorting between the phases. Two high current arcing events were observed on SPENCER. Both events clipped at the 300-A limit of the NILM current sensors. The first event lasted for about six line cycles and occurred while the heater was drawing the nominal 4.5 kW. All three phases experience a large current spike, as shown in Fig. 7(a). Arcing is known to cause distortions in the voltage waveform near the zero crossings [21], as is evident in Fig. 7(b). The second arcing event occurred ≈9 h later and lasted for about 22 line cycles. In the interval between the arcing events, two heating elements open-circuited. Thus, in the second arcing event, only the *ca* element is operating, and only phases *c* and *a* experience spikes in current. A section of the current and voltage streams is shown in Fig. 8(a) and (b), respectively. Both high current arcing events are attributed to the JW heater, because the currents return to normal levels with the turn-off of the JW heater.

The heaters are supplied from a 15-A breaker with an instantaneous trip rating of 180–750-A rms. The trip rating depends on both the current magnitude and event duration. Using curve fitting on the clipped current data to estimate the true current magnitude, it was estimated that both events fell between the breaker's minimum and maximum clearing times. An exact magnitude cannot be determined because of the clipping and distortions around the zero crossing, but the estimate indicates that the breaker likely did not trip during these events. This was corroborated by speaking with watchstanders onboard the vessel and confirmed that they had no indication that these arcing events occurred or of any breakers having tripped. The standard protection and relaying on this power system failed to catch the dangerous arcing that was easily observed by the NILM.

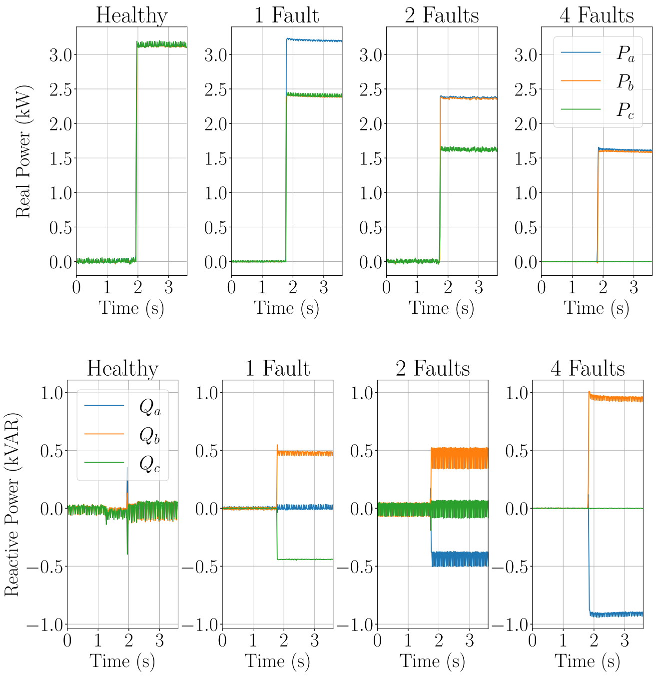

Fig. 6. Per-phase real power (top) and reactive power (bottom) of the SPENCER port-side heater turn-on events, starting healthy and after the heater underwent various stages of degradation.

C. High-Impedance Ground Fault

The sheathing of the JW heaters is grounded. Damaged sheathing and a damaged heating element may lead to a ground fault. The detection and location of ground faults are necessary for power utilization safety. The shipboard system

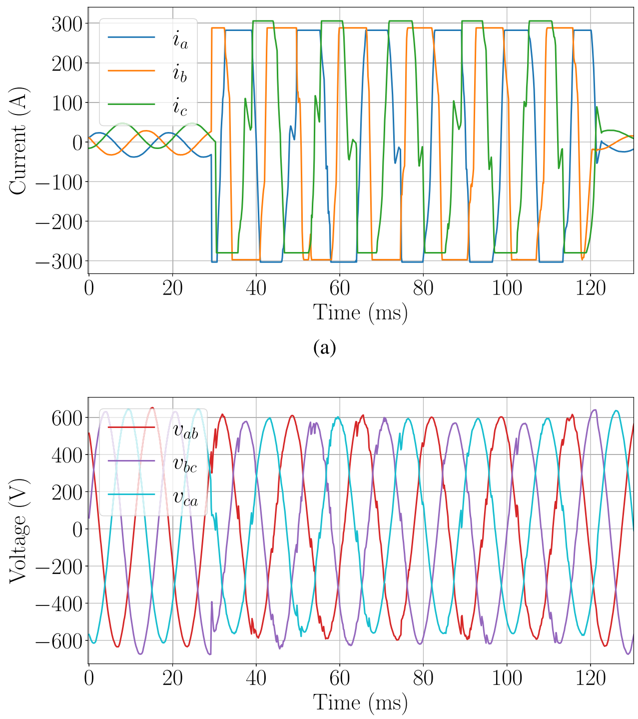

(b)

Fig. 7. (a) Currents and (b) voltages during the first arcing event, in which all three line currents spike. There are visible distortions in the voltage waveform.

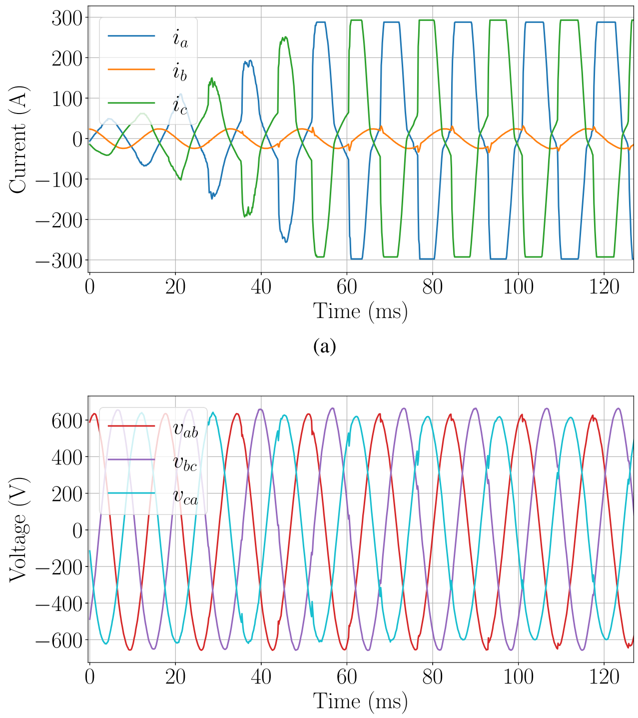

(b)

Fig. 8. (a) Currents and (b) voltages during the second arcing event, in which phases a and c show current spikes.

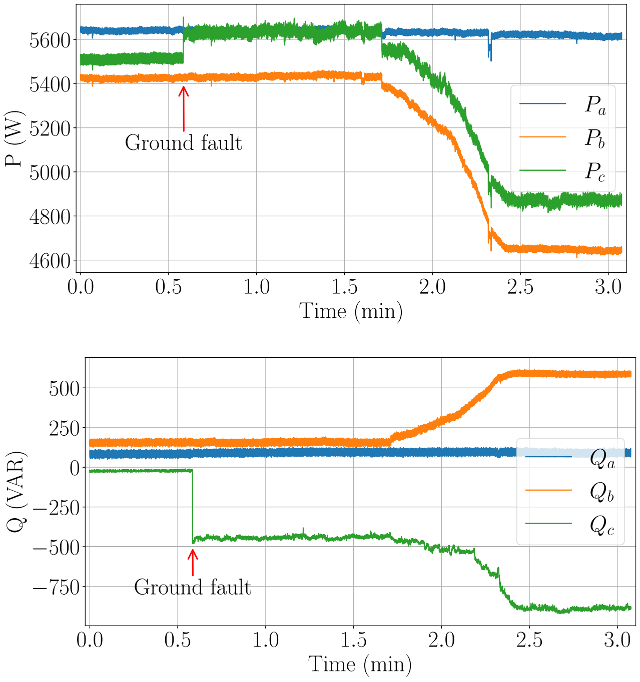

Fig. 9. Aggregate real power and reactive power with a phase c ground fault at 0.6 min immediately followed by a degrading bc heating element.

is nominally an ungrounded system. In reality, the system is capacitively grounded through the parasitic, or natural capacitances of three-phase conductors and other distribution equipment to ground (i.e., the vessel's hull). In an ungrounded system, a single line-to-ground fault does not cause any service disruptions, instead a shifting of the neutral occurs. If a phase conductor makes solid contact with ground, it equates the faulted phase and ground potential. It also raises the voltage of the other two phases to ground from V to $\sqrt{3}$ V [22]. Ground faults often occur with some resistance associated with the fault. The presence of a fault resistance affects the line-to-ground voltage shift and fault current magnitude. As the fault resistance increases, the change in line-to-ground voltage decreases, and the fault current decreases. These ground faults are "high-impedance" faults. High-impedance faults are difficult to detect and locate due to the smaller current magnitude [23], [24]. The fault current magnitudes may be similar to those of normal loads. Thus, normal overcurrent protection devices may not detect and clear these faults. Instead, detection of a ground fault is often performed with a zero-sequence voltage relay [23]. Locating ground faults requires the manual sequential opening of branch circuits until the fault disappears. As will be described, a ground fault manifests as a unique power signature. Thus, a NILM can detect ground faults and supplement existing protection schemes.

Two line-to-ground faults were observed on SPENCER. Fig. 9 shows the aggregate power stream of one observed fault. There is a ground fault on phase c at $t = 0.6$ min, appearing as a step change in P_c and Q_c of ≈109 W and −437 VAR, respectively. There is no significant change in power on the other two phases. This is expected, since the current through the fault resistance is measured in the line current of the faulted phase. With no fault resistance, it is a purely capacitive current, and a negative Q is added to the aggregate power stream of the faulted phase. With a fault resistance, the ground fault also adds a positive P to the faulted phase.

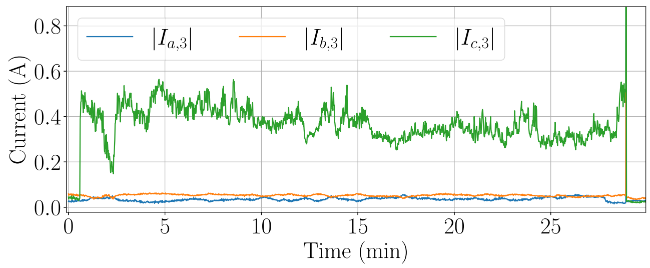

Fig. 10. Third-harmonic rms current envelopes during a phase c ground fault.

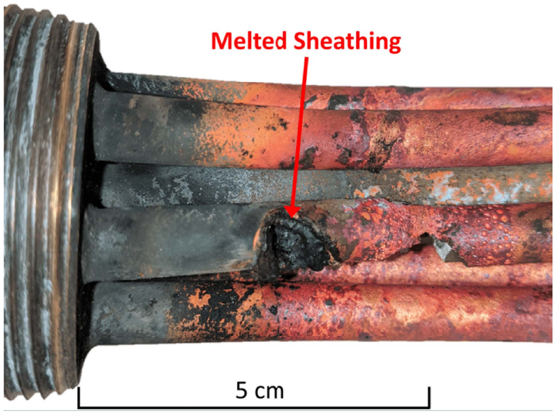

Fig. 11. After the crew was alerted to arcing observed with the NILM, the heater was removed from the engine block, showing significant damage, including bent elements and melted sheathing.

Fig. 10 shows the magnitude of the rms third-harmonic current envelope for the ≈30 min duration of the observed ground fault. The increase in the third-harmonic current only occurs on the faulted phase (phase c). The step change in the third-harmonic current at $t = 0.6$ min in Fig. 10 corresponds to the step change in power in Fig. 9. The third-harmonic current on phase c returns to ≈0 at about $t = 29$ min in Fig. 10 when the faulted heater turns off. This is expected behavior, as the ground fault provides a low-impedance path for zero-sequence components, which are normally circulating around the delta. For a balanced load, the third-harmonic and other triplen currents are zero sequence.

This ground fault was immediately followed by the deterioration and resulting open circuit of the bc heating element of the JW heater, appearing as a slow change in power until $t = 2.4$ min in Fig. 9. Before the ground fault cleared, another heating element deteriorated (the ab element). This was immediately followed by a high-current arcing event (see Fig. 8). Both the ground fault and high current arcing were cleared with the subsequent turn-off of the heater. After being removed from the engine block, this heater showed significant damage, oxidation, scale formation, pitting, and melted sheathing, as shown in Fig. 11.

IV. ROOT-CAUSE FAILURE ANALYSIS AND DISCUSSION

The electrical signatures presented in Section III are effective in identifying degraded heater operation, but cannot fully explain what is causing the faults. To assist with this evaluation, a material analysis of failed JW heaters was conducted. The material analysis revealed possible stress corrosion cracking (SCC) of the copper sheathing. To further investigate the possibility of SCC, the induced stress from engine vibration was estimated. A vibration analysis was conducted for estimating the heater's natural frequency. This section presents the material, stress, and vibration root-cause failure analysis. The induced stress and natural frequency evaluations leverage Autodesk's finite-element analysis (FEA) software. All FEA simulations assume ideal geometry of a new heater, ignore effects of the heating wire and insulating powder within the heating elements, and use fixed-free boundary conditions with the heating elements fixed perpendicular to the base and free opposite the base. Heater specifications and inspection informed use of wrought copper with the following mechanical properties in both FEA simulations: Young's modulus of 118 GPa, Poisson's ratio of 0.345, yield strength of 70.0 MPa, and ultimate tensile strength of 220 MPa. This section then connects the root-cause analysis to the electrical analysis to identify how nonintrusive load monitoring measurements can be used to detect the analyzed failure modes.

A. Material Analysis

Postmortem analysis of failed heating elements revealed significant corrosion, both general and pitting, as well as possible SCC of the copper sheathing. Computed tomography (CT) imaging of a heater was conducted using the Nikon XT H 225 Stand instrumentation, with the VGStudio Max software for visualization. The CT showed significant material loss in addition to through-wall cracking, as shown in Fig. 12. The area highlighted in the CT analysis was on a sheath section that did not appear to have been directly involved in a shorting event. Neighboring sections of sheathing experienced significant melting and material loss. These areas were avoided in the CT analysis due to the expected material damage and the desire to observe the condition of the copper prior to an arcing event. The analyzed area would have been thermally isolated from the short by the JW it was submersed in.

The copper heating element sheath is electrically isolated from the iron chrome aluminum (FeCrAl) heating wire by magnesium oxide (MgO) powder. A breach in the sheathing by through-wall pitting and cracking can cause infiltration of the insulating MgO powder with JW. One contributing factor in the cracking of the copper sheathing may actually have been in the selection of corrosion inhibitor for the JW. An additive rich in nitrites was used to inhibit corrosion, with concentrations hovering around 1000 ppm, as shown in Fig. 13. Scientific literature demonstrates that copper exposed to nitrites may induce SCC [25], [26]. The loss of wall thickness and the presence of large pits shown in Fig. 12 suggests that cracking is one possible route for JW to enter the insulator. In our analysis, the cracked regions were the only areas, outside of the obvious arc locations, in which through-wall perforations in the sheathing were observed.

As mentioned, through-wall pitting and cracking of the sheathing may allow JW into the insulating MgO powder. The result of JW ingress into the insulator was observed in

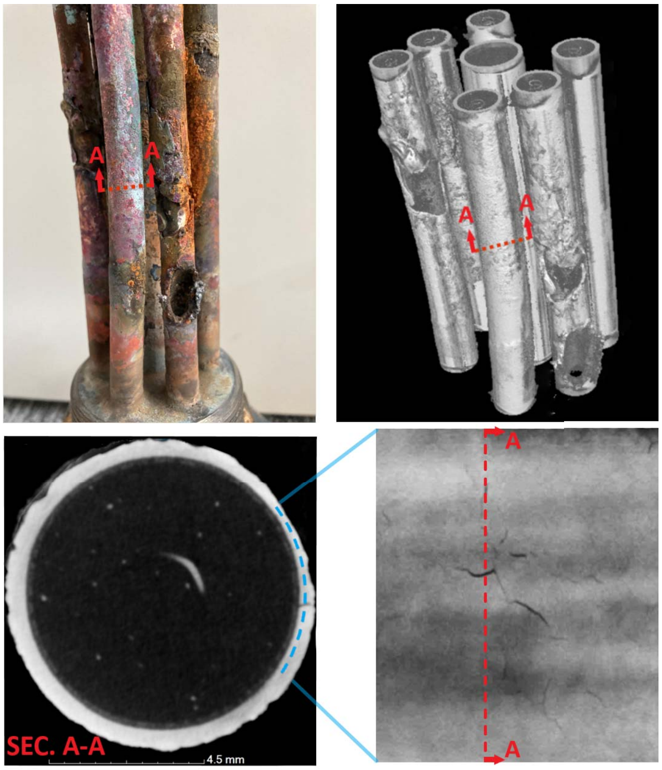

Fig. 12. Top left—degraded JW heater from ESCANABA. Top right—CT scan of heater, 3-D volume reconstruction, and high density materials appear bright in contrast. Bottom left—virtual cross section showing through wall crack at 3 o'clock. Bottom right—virtual unrolling of sheathing showing branched network of cracking. Dashed lines—plane of cross section and unrolling.

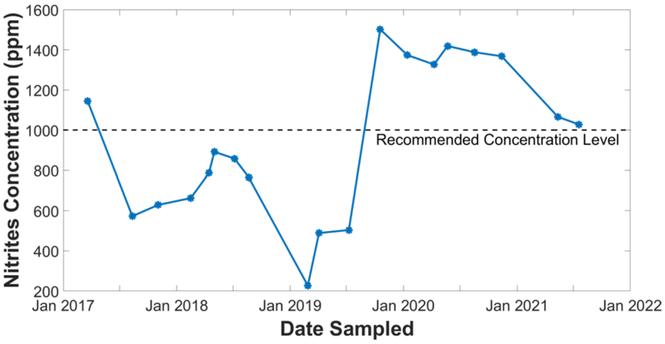

Fig. 13. ESCANABA JW chemistry from March 2017 to May 2021.

scanning electron microscopy (SEM) and energy-dispersive X-ray spectroscopy (EDS), which is shown in Fig. 14. The dark void through the copper sheathing in Fig. 14 is the crack from Fig. 12. Preferential deposition of copper through the insulating MgO powder toward the energized heating element was observed. Continued growth of the copper phase through the insulator could explain the shorting experienced and the significant arc damage observed in the failed heating elements.

B. Induced Stress Determination

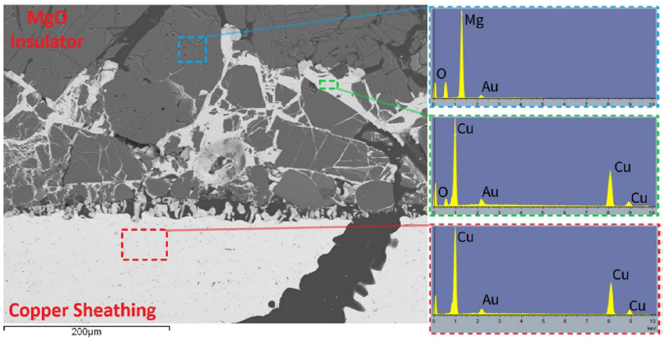

Fig. 14. SEM/EDS of the interior surface of the sheathing showing preferential growth of a copper-rich phase (green/middle box) toward the energized heating element.

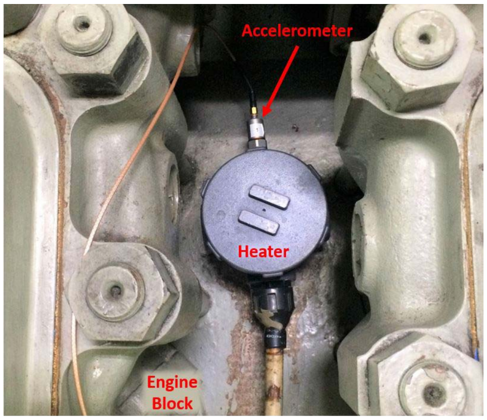

Fig. 15. Configuration for monitoring vibration of installed JW heater.

To further evaluate the possibility of SCC, the induced stress from engine vibration was predicted with analytic equations and FEA software. The JW heater consists of a housing and three heating elements. The housing threads directly into the MPDE block. The heating elements resemble a set of cantilever beams or prongs of a tuning fork and react similarly to disturbances or impulses. For both the analytic and FEA methods, the JW heater was modeled as a cantilever beam with fixed-free boundary conditions, and a force vector was used, which was derived from accelerometer measurements of a JW heater while installed on a running MPDE. The vibration was measured using a single axis accelerometer affixed to the side of the heater housing, as shown in Fig. 15, and the DAQ device discussed in [27]. The accelerometer used has a sensitivity of 505 mV/g and an output range of 0–5 V. These vibration measurements recorded a sinusoidal waveform that cycled at 1640 Hz and reached an amplitude of 44.3 N. For the analytical induced stress determination, this force was distributed across the length of a heating element, as shown in Fig. 16. This free body diagram depicts heater orientation as installed in an engine block and forces exerted on the heater. Hydrostatic pressure due to submergence in JW, F_{Hydro}, is represented in blue, a distributed load that emulates engine vibration, F_{Vibe}, is represented in orange, and a heating element weight vector, mg, is represented in black. To simplify analytical calculations, the hydrostatic pressure and element weight due to gravity were assumed negligible in comparison with the effects of the vibration force. A later comparison

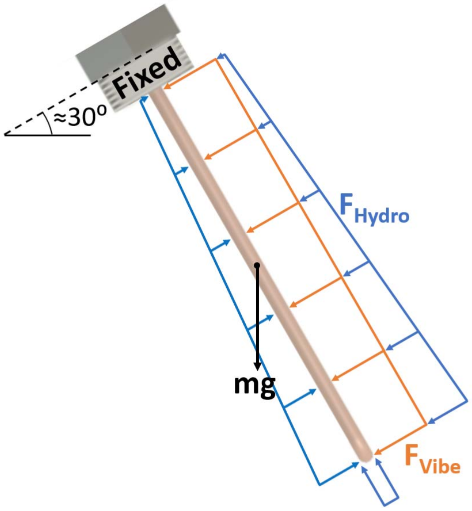

Fig. 16. Free body diagram of heater modeled as a cantilever beam. For visual clarity, only a single heating element is shown, and force vectors are not drawn to scale.

with FEA results validates the use of these assumptions for the analytical stress determination.

Stress develops in beams due to shear and bending action. Both shear and bending stress factor into the resultant principal stress experienced by the heater. To determine these, the shear force and bending moment along the length of the heater must be known. Shear stress, τ, is defined as

$$\tau = \frac{2V_x}{A} \tag{4}$$

where V_x is the shear force, and A is the cross-sectional area of the beam. The vertical shear caused by a uniformly distributed load, w, along a cantilever beam is defined as

$$V_x = w(l - x) \tag{5}$$

where l is the length of the beam, and x is the distance from the beam's fixed end to the point being evaluated [28]. Bending stress, σ, is defined as

$$\sigma = \frac{M_x y}{I} \tag{6}$$

where M_x is the induced bending moment, y is the distance from the beam's neutral axis, and I the beam's moment of inertia [28]. For all calculations, y was selected to evaluate the outer most fiber of a heating element where stress will be greatest. The bending moment caused by a uniformly distributed load, w, along a cantilever beam is defined as

$$M_x = \frac{1}{2} w (l - x)^2. \tag{7}$$

Using an F_{Vibe} of 153 N/m, the shear stress, bending stress, and resultant principal stress were determined at 44 points along the heating element's length, with a higher concentration of points near its base where higher stress is anticipated. These calculations predict a maximum stress of 90.9 MPa at the heating element's base. Fig. 17 depicts these results as a percentage of maximum induced principal stress. At the base, principal stress starts at a maximum and gradually decreases to nearly zero at the heating element's free end.

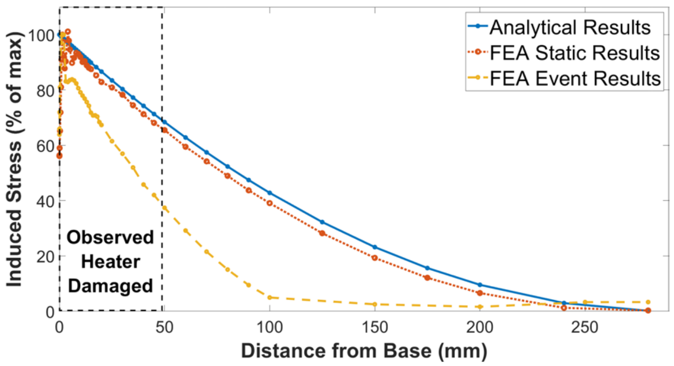

Fig. 17. Induced heater element stress comparison of analytical and FEA results showing largest induced stress near the heater's base.

To verify analytical stress predictions, a model of the JW heater was generated and assessed using Autodesk's finite-element static stress simulator. This analysis used a scaled tetrahedral mesh based on 4% of component size with more than 40 000 elements. In addition to the distributed vibration load used for the analytical determination, a hydrostatic pressure equivalent to 3 m of water was placed over the heating elements to emulate the submerged condition of an installed heater, and gravity was considered as part of the simulation. The simulation results are shown in Fig. 18(a) and found that induced stress from engine excitation is greatest near the base of the heating element and diminishes along the element's length. A maximum induced stress of 86.2 MPa was observed ≈4 mm from the heater's base. These results are plotted in Fig. 17, which show a close relation between the analytic and FEA static stress determination methods. It is expected that further mesh refinement would likely resolve the erratic FEA results within 4 mm of the heater's base.

The static stress FEA validates analytical results, but more complex simulations are available through Autodesk FEA software, specifically, an event simulator that can apply time-dependent cyclic loads. Based on the same heater vibration measurements described before, a sinusoidal load that cycles at 1640 Hz and reaches an amplitude of ±44.3 N was applied perpendicular to the element's arched plane at its center of mass for the event simulation. This analysis used an adaptive tetrahedral mesh with more than 43 000 elements and incorporated the same hydrostatic pressure and gravity forces used for the static stress FEA. Simulation results at the moment of peak impulse, +44.3 N, are plotted in Fig. 17. The stress profile from the FEA event simulation resembles those of the previous stress determination methods with greatest stress near the heater's base, but drops off quicker than the other methods. This disparity is likely due to the frequency at which the time-dependent vibration force is applied during the FEA event simulation. A shift from +44.3 to −44.3 N over a time span of 0.003 s does not allow stress to fully develop along the length of an element prior to reversing direction.

These analytical and FEA simulation stress determination findings align with holes that have been observed to typically occur within 5 cm of the heater's base, as shown for two

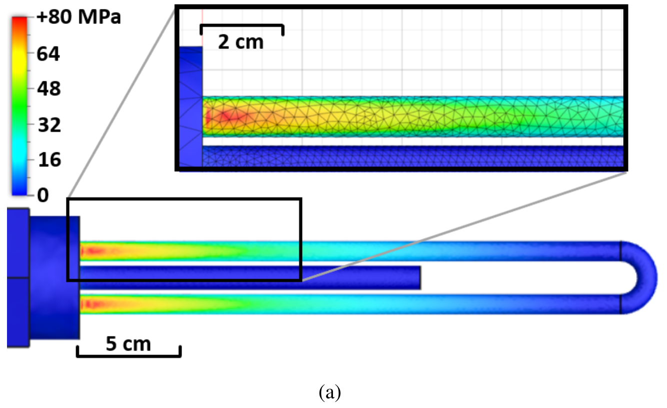

(a)

(b)

Fig. 18. Finite-element static stress simulation and observed damage. (a) Stress simulation results, color gradient in MPa. (b) Holes observed at ≈1 and 5 cm from the heater's base.

example heaters in Fig. 18(b). That is, observed holes are close to the heater's base, where induced principal stress is highest. This distance range is also highlighted on the induced heater element stress line plot in Fig. 17.

C. Natural Frequency Determination

The development of SCC can be partially attributed to continuous exposure to high concentrations of nitrites and the induced stress from engine vibration. Excitation at the heater's natural frequency may induce resonance that could accelerate the process. To evaluate this potential, in this section, the heater's natural frequency is estimated and compared with the MPDE's operating speed. The natural frequency of the JW heater was predicted with the measurement of physical parameters and analytic equations, and then was verified experimentally.

First, physical parameters of the JW heater were measured using a deflection experiment. The deflection experiment was conducted on a single heating element with known weights and a dial indicator. The shape of the heating elements complicates separate calculation of the second moment of area, I, and Young's modulus of elasticity, E. Instead, the product EI was determined with

$$EI = \frac{Fl^3}{3\delta} \tag{8}$$

where F is the applied force, l is the length, and δ is the deflection [29], [30]. This is the deflection equation for a cantilever beam (boundary conditions fixed-free) with a point load applied at the free end. Point loads ranging from 1.7 to 4.5 N were applied 26 cm from the fixed end of the heating element. This resulted in an average EI value of 62.2 $\mathrm{N \cdot m^2}$. It was ensured that loading of the heating element remained within the elastic region of the component's stress–strain curve by verifying it returned to its neutral position after removing the applied load. Deflection from the heating element's own weight was deemed negligible, as it was calculated to be less than 1% of the total deflection.

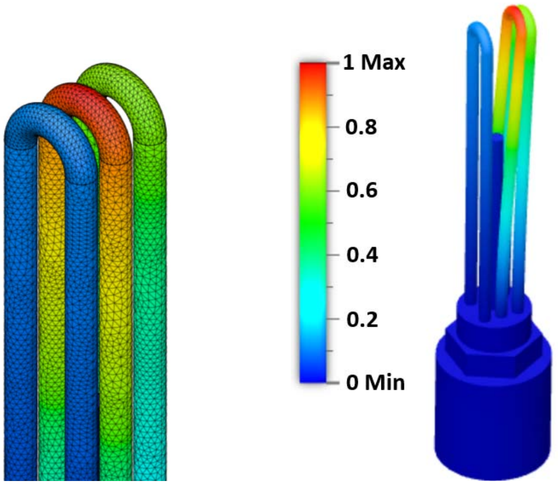

(a) (b)

Fig. 19. Natural frequency modeling using FEA. (a) Finite-element mesh and (b) natural frequency simulation, color gradient indicating relative displacement.

For determining the natural frequency of the element, its own mass must be considered. Based on CT scanning and EDS performed during the material analysis, the heating element's mass per unit length was determined to be 0.33 kg/m and was confirmed by cutting and weighing a small section of the heating element. The natural frequency, f, of a heating element was calculated with

$$f = 0.56\sqrt{\frac{EI}{ql^4}} \tag{9}$$

where q is the mass per unit length [29]. This provided a predicted first-order natural frequency of 93.6 Hz for a single heating element. Due to the rigidity of the housing, mounting configuration, and overall slenderness of individual elements, higher order modulations and interactions between elements were not considered. To further evaluate these considerations, a computer-aided design (CAD) model was generated and assessed using Autodesk's finite-element modal frequency analysis. A scaled tetrahedral mesh based on 10% of component size with more than 175 000 elements was used and is shown in Fig. 19(a). Results of the analysis indicated a primary natural frequency at 96.8 Hz with the center heating element oscillating in the same plane as the outer two, as shown in Fig. 19(b).

To verify the predicted natural frequency values generated from the physical parameter calculations and the FEA, an impulse impact experiment was conducted. The experiment was conducted for two scenarios, an undamped case,

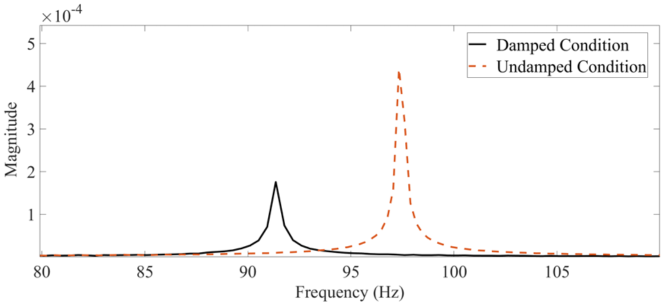

Fig. 20. DFTs to determine JW heater natural frequency in damped and undamped conditions.

TABLE I
NATURAL FREQUENCY—NEW HEATER

Method	Frequency
Deflection Experiment	93.6 Hz
CAD Model	96.8 Hz
Hammer Impact (Undamped)	97.3 Hz
Hammer Impact (Damped)	91.3 Hz

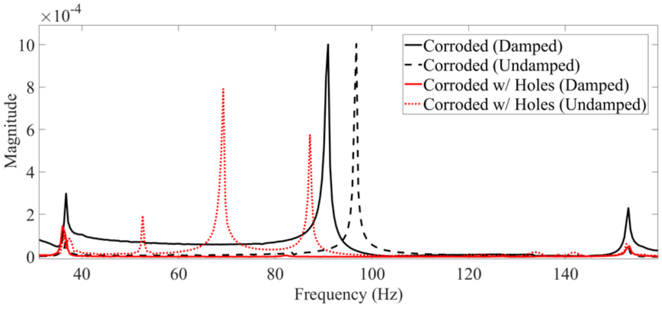

Fig. 21. DFTs to determine corroded JW heater natural frequency in damped and undamped conditions.

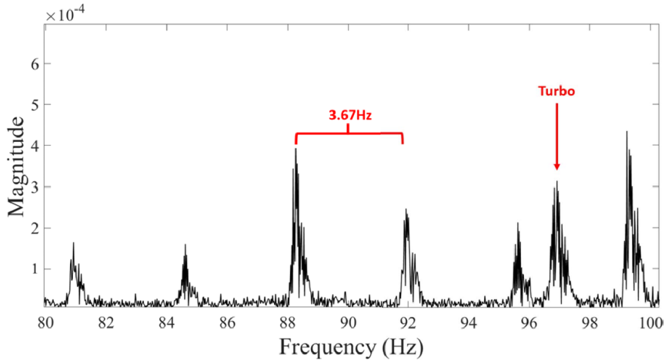

Fig. 22. DFT of monitored vibration of JW heater with MPDE idling.

i.e., an unsubmerged heater, and a damped case, i.e., a heater submerged in water. The damped case simulates the actual operating condition of the heater. The vibration of the heater was measured with the previously discussed accelerometer affixed to the side of the heater housing. An impulse impact was used to excite the system [31], and the DFT of the responses is shown in Fig. 20. For the undamped system, the response shows a peak at 97.3 Hz. This result closely matches predicted values and verifies the deflection experiment and analytic formulation. For the damped system, the response shows a smaller, but still prominent peak at 91.3 Hz. The natural frequencies as predicted by the deflection experiment, CAD model, and impulse impact tests are summarized in Table I.

The impulse impact method was also used on JW heaters with visible signs of deterioration. The DFT of the responses is shown in Fig. 21. For the corroded heater without holes, the primary response shows a peak at 90.9 and 96.8 Hz in the damped and undamped conditions, respectively. These closely resemble the peaks of the new heater. However, smaller peaks are also present around 36 and 153 Hz. For the corroded heater with holes, there is a more prominent shift in DFT peaks. In the damped condition, there is no longer a primary peak around 90–98 Hz. Instead, there are small peaks at 36 and 153 Hz. In the undamped condition, there are substantial peaks at 87.2 and 69.3 Hz, with minor peaks around 36, 53, and 153 Hz. These varying results are anticipated, because any imperfections in the heating element caused by corrosion or heating will impact the structure's natural frequency.

Field vibration measurements were gathered while the MPDE was idling at 440 rpm. These measurements were used to investigate possible excitation of the heaters during operation. An accelerometer was attached to the heater housing, as shown in Fig. 15, in the same manner as in the laboratory hammer impact experiment. Measurements were also taken with the accelerometer attached directly to the MPDE block. Both measurements present a vibration spectrum that is rich in content due to phenomena, such as cylinder firing, shaft rotation, possible imbalances, misalignment, and other non-idealities associated with mechanical systems. However, the spectrum is dominated by the fundamental engine order of 3.67 Hz and its subsequent harmonics. A peak was also observed at 97 Hz in measurements from both the JW heater and MPDE block. Based on vibration measurements gathered directly from the engine's turbo, this peak was determined to be a harmonic of the turbo's rotational speed. The DFT of a JW heater measurement is shown in Fig. 22. It is suspected that the impulses imparted by the MPDE onto the JW heater near the calculated natural frequency values presented previously (see Table I) are likely to trigger heater resonance excitation [32]. For a healthy heater, with undamaged copper sheathing, resonant excitation due to engine vibration is unlikely to cause failure. However, if the copper sheathing is weakened due to corrosion or a manufacturer defect, resonant excitation could exacerbate structural pathologies and induce SCC.

D. Detection of a Degraded Heater

A NILM cannot directly diagnose the discussed failure modes, such as SCC and damaged sheathing. However, it can detect the associated electrical failures, such as open circuits, arcing, and high-impedance ground faults. Detection of the described electrical failures provides an indicator that gives advanced warning to the ship's crew of possible damage. Early detection of these failures and subsequent action can prevent further damage and eliminate potentially dangerous operating conditions for the ship's crew.

These faults have power signatures that can be explained by the physics of power system behavior. An open-circuited heating element can be detected by the predicable changes in P and Q. However, these events are difficult for a machine learning classifier to detect if only trained on healthy load data. A NILM pattern classifier can be trained to recognize these failure events using simulated degraded load transients. An arcing event can be detected by the sudden high current and power magnitudes. For the high-impedance ground fault, the step change in power is similar in magnitude to those of normal loads. However, the transient patterns of this fault are unique. In a delta distribution system, no load draws a line current on only a single phase. Even a single-phase line-to-line load will draw line currents on two phases. Thus, a step change in power on only a single phase and an increase in third-harmonic on that same phase potentially indicates a ground fault. If the ground fault is due to a faulty load, the location can be narrowed down based on the energized loads as given by a NILM load identifier.

V. CONCLUSION

Electrical analysis with nonintrusive load monitoring unveiled degraded MPDE JW heater power signatures, arcing, and high-impedance ground faults. Diagnostic signatures developed for electrical monitoring can be used to detect material degradation and structure failure. Subsequent removal and inspection of the heaters in our field tests revealed corrosion, arcing, melting, and cracking of the heating elements. Monitoring the JW heaters for corrosion and related damage is critical to ensure the efficient and safe operation of the JW keep-warm system. Power monitoring can alert watchstanders to possible corroded heating elements and prevent progressively worsening safety hazards. It can also be used to streamline maintenance activities, using power stream data as a metric for conducting condition-based maintenance, rather than recurring preventative maintenance.

ACKNOWLEDGMENT

The authors would like to thank the United States Coast Guard (USCG) and, in particular, the crews of USCG cutter (USCGC) SPENCER and USCGC ESCANABA for granting access to their ships.

REFERENCES

[1] J. Ge, F. Yu, T. Tomizawa, H. Song, and N. Yusa, "Inspection of pitting corrosions on weld overlay cladding using uniform and rotating eddy current testing," *IEEE Trans. Instrum. Meas.*, vol. 70, pp. 1–10, 2021.

[2] D. C. Sweeney, A. M. Schrell, and C. M. Petrie, "Pressure-driven fiber-optic sensor for online corrosion monitoring," *IEEE Trans. Instrum. Meas.*, vol. 70, pp. 1–10, 2021.

[3] B. Gustavsen, M. Hoyer-Hansen, M. Hatlo, and S. Midttveit, "Voltages and AC corrosion on metallic tubes in umbilical cables caused by magnetic induction from power cable charging currents," *IEEE Trans. Power Del.*, vol. 34, no. 2, pp. 596–605, Apr. 2019.

[4] J. R. Gallion and R. Zoughi, "Millimeter-wave imaging of surface-breaking cracks in steel with severe surface corrosion," *IEEE Trans. Instrum. Meas.*, vol. 66, no. 10, pp. 2789–2791, Oct. 2017.

[5] T. Kane, "The NILM dashboard: Shipboard automatic watchstanding and real-time fault detection using non-intrusive load monitoring," M.S. thesis, Dept. Mech. Eng., Massachusetts Inst. Technol., Cambridge, MA, USA, 2019.

[6] F. Ciancetta, G. Bucci, E. Fiorucci, S. Mari, and A. Fioravanti, "A new convolutional neural network-based system for NILM applications," *IEEE Trans. Instrum. Meas.*, vol. 70, pp. 1–12, 2021.

[7] J. Alcalá, J. Ureña, Á. Hernández, and D. Gualda, "Event-based energy disaggregation algorithm for activity monitoring from a single-point sensor," *IEEE Trans. Instrum. Meas.*, vol. 66, no. 10, pp. 2615–2626, Oct. 2017.

[8] W. Luan, Z. Liu, B. Liu, Y. Yu, and Y. Hou, "An adaptive two-stage load event detection method for nonintrusive load monitoring," *IEEE Trans. Instrum. Meas.*, vol. 71, pp. 1–14, 2022.

[9] M. Kaselimi, N. Doulamis, A. Voulodimos, E. Protopapadakis, and A. Doulamis, "Context aware energy disaggregation using adaptive bidirectional LSTM models," *IEEE Trans. Smart Grid*, vol. 11, no. 4, pp. 3054–3067, Jul. 2020.

[10] E. Azizi, M. T. H. Beheshti, and S. Bolouki, "Appliance-level anomaly detection in nonintrusive load monitoring via power consumption-based feature analysis," *IEEE Trans. Consum. Electron.*, vol. 67, no. 4, pp. 363–371, Nov. 2021.

[11] E. K. Saathoff, D. H. Green, R. A. Agustin, J. W. O'Connell, and S. B. Leeb, "Inrush current measurement for transient space characterization and fault detection," *IEEE Trans. Instrum. Meas.*, vol. 70, pp. 1–10, 2021.

[12] P. A. Lindahl, D. H. Green, G. Bredariol, A. Aboulian, J. S. Donnal, and S. B. Leeb, "Shipboard fault detection through nonintrusive load monitoring: A case study," *IEEE Sensors J.*, vol. 18, no. 21, pp. 8986–8995, Nov. 2018.

[13] H. Rashid, P. Singh, V. Stankovic, and L. Stankovic, "Can non-intrusive load monitoring be used for identifying an appliance's anomalous behaviour?" *Appl. Energy*, vol. 238, pp. 796–805, Mar. 2019.

[14] J. Paris, J. S. Donnal, R. Cox, and S. B. Leeb, "Hunting cyclic energy wasters," *IEEE Trans. Smart Grid*, vol. 5, no. 6, pp. 2777–2786, Nov. 2014.

[15] D. Green, T. Kane, S. Kidwell, P. Lindahl, J. Donnal, and S. Leeb, "NILM dashboard: Actionable feedback for condition-based maintenance," *IEEE Instrum. Meas. Mag.*, vol. 23, no. 5, pp. 3–10, Aug. 2020.

[16] A. Aboulian *et al.*, "NILM dashboard: A power system monitor for electromechanical equipment diagnostics," *IEEE Trans. Ind. Informat.*, vol. 15, no. 3, pp. 1405–1414, Mar. 2019.

[17] *UE9 Datasheet*, Labjack Corporation, Lakewood, CO, USA, 2020.

[18] J. Paris, J. S. Donnal, and S. B. Leeb, "NilmDB: The non-intrusive load monitor database," *IEEE Trans. Smart Grids*, vol. 5, no. 5, pp. 2459–2467, Sep. 2014.

[19] J. Paris, J. S. Donnal, Z. Remscrim, S. B. Leeb, and S. R. Shaw, "The sinefit spectral envelope preprocessor," *IEEE Sensors J.*, vol. 14, no. 12, pp. 4385–4394, Dec. 2014.

[20] W. Wichakool, A. T. Avestruz, R. W. Cox, and S. B. Leeb, "Modeling and estimating current harmonics of variable electronic loads," *IEEE Trans. Power Electron.*, vol. 24, no. 12, pp. 2803–2811, Dec. 2009.

[21] A. van Deursen, P. Wouters, and F. Steennis, "Corrosion in low-voltage distribution networks and perspectives for online condition monitoring," *IEEE Trans. Power Del.*, vol. 34, no. 4, pp. 1423–1431, Aug. 2019.

[22] D. Paul, "Phase-ground fault current analysis and protection of a high-resistance grounded power system," *IEEE Trans. Ind. Appl.*, vol. 56, no. 4, pp. 3306–3314, Jul. 2020.

[23] T. Baldwin and F. Renovich, "Analysis of fault locating signals for high-impedance grounded systems," *IEEE Trans. Ind. Appl.*, vol. 38, no. 3, pp. 810–817, May 2002.

[24] M. Wei, W. Liu, H. Zhang, F. Shi, and W. Chen, "Distortion-based detection of high impedance fault in distribution systems," *IEEE Trans. Power Del.*, vol. 36, no. 3, pp. 1603–1618, Jun. 2021.

[25] G. Mori, D. Scherer, S. Schwentenwein, and P. Warbichler, "Intergranular stress corrosion cracking of copper in nitrite solutions," *Corrosion Sci.*, vol. 47, no. 9, pp. 2099–2124, 2005.

[26] M. B. Kannan and P. Shukla, "Stress corrosion cracking (SCC) of copper and copper-based alloys," in *Stress Corrosion Cracking* (Woodhead Publishing Series in Metals and Surface Engineering), V. Raja and T. Shoji, Eds. Sawston, U.K.: Woodhead Publishing, 2011, pp. 409–426.

[27] L. Huchel, T. C. Krause, T. Lugowski, S. B. Leeb, and J. Helsen, "Chasing the cut: A measurement approach for machine tool condition monitoring," *IEEE Trans. Instrum. Meas.*, vol. 70, pp. 1–10, 2021.

[28] J. E. Shigley and C. R. Mischke, *Mechanical Engineering Design*, 5th ed. New York, NY, USA: McGraw-Hill, 2008.

[29] S. H. Crandall, N. C. Dahl, and T. J. Lardner, *An Introduction to the Mechanics of Solids*, 2nd ed. New York, NY, USA: McGraw-Hill, 1999.

[30] R. D. Blevins, *Formulas for Natural Frequency and Mode Shape*, 1st ed. New York, NY, USA: Van Nostrand Reinhold Co, 1977.

[31] A. Omekanda, Z. Tang, and P. Pillay, "Vibration prediction in switched reluctance motors with transfer function identification from shaker and force hammer tests," *IEEE Trans. Ind. Appl.*, vol. 39, no. 4, pp. 978–985, Jul./Aug. 2003.

[32] B. Cornwell, *Modern Physics With Waves, Thermodynamics, and Optics*. Fullerton, CA, USA: Light and Matter, 2021.

Daisy H. Green (Member, IEEE) received the B.S. degree in electrical engineering from the University of Hawaiʻi at Mānoa, Honolulu, HI, USA, in 2015, and the M.S. and Ph.D. degrees in electrical engineering and computer science from the Massachusetts Institute of Technology (MIT), Cambridge, MA, USA, in 2018 and 2022, respectively.

She is currently a Post-Doctoral Associate with MIT. Her research interests include the development of signal processing algorithms for energy management and condition monitoring.

Devin W. Quinn received the M.S. degree in mechanical engineering from the Massachusetts Institute of Technology, Cambridge, MA, USA, in 2022.

He was previously stationed as a Damage Control Officer aboard United States Coast Guard cutter (USCGC) DILIGENCE and an Engineer Officer onboard USCGC ESCANABA. He is currently a Lieutenant Commander with the United States Coast Guard, Alameda, CA, USA.

Samuel Madden received the Ph.D. degree in materials science and engineering from the University of Virginia, Charlottesville, VA, USA, in 2014.

He is currently a Managing Engineer with the Materials and Corrosion Engineering Practice, Exponent, Inc., Natick, MA, USA.

Peter A. Lindahl (Senior Member, IEEE) received the B.S. degree in electrical engineering from Penn State University, State College, PA, USA, in 2003, and the M.S. degree in electrical engineering and the Ph.D. degree in engineering from Montana State University, Bozeman, MT, USA, in 2009 and 2013, respectively.

He is currently a Manager with the Electrical Engineering Practice, Exponent, Inc., Natick, MA, USA, where he is involved in providing technical consulting services in the areas of root-cause failure analysis, product safety and performance assessments, and intellectual property audits for a wide range of electrical, electromechanical, and energy storage systems.

Steven B. Leeb (Fellow, IEEE) received the Ph.D. degree from the Massachusetts Institute of Technology (MIT), Cambridge, MA, USA, in 1993.

He holds a joint appointment with the Department of Mechanical Engineering, MIT. He is concerned with the development of signal processing algorithms for energy and real-time control applications.

Dr. Leeb has been a member on the MIT Faculty with the Department of Electrical Engineering and Computer Science, since 1993.